Effect of crystal orientation on microstructure and properties of bulk Fe_2B intermetallic

Shengqiang Ma,[a] Zhifu Huang, Jiandong Xing, and Guangzhu Liu
State Key Laboratory for Mechanical Behavior of Materials, School of Materials Science and Engineering, Xi'an Jiaotong University, Xi'an, Shaanxi Province 710049, People's Republic of China

Yaling He
MOE Key Laboratory of Thermo-Fluid Science and Engineering, School of Energy and Power Engineering, Xi'an Jiaotong University, Xi'an, Shaanxi Province 710049, People's Republic of China

Hanguang Fu
Research Institute of Advanced Materials Processing Technology, School of Materials Science and Engineering, Beijing University of Technology, Beijing 100124, People's Republic of China

Yong Wang and Yefei Li
State Key Laboratory for Mechanical Behavior of Materials, School of Materials Science and Engineering, Xi'an Jiaotong University, Xi'an, Shaanxi Province 710049, People's Republic of China

Dawei Yi
School of Materials Science and Engineering, Xi'an University of Science and Technology, Xi'an, Shaanxi Province 710054, People's Republic of China

(Received 12 September 2014; accepted 1 December 2014)

The effects of Fe_2B-grain orientation on microstructure and properties of bulk Fe_2B intermetallic fabricated by directional and ordinary solidification techniques have been investigated. The results show that unidirectional solidified Fe_2B intermetallic possesses a strong (002) texture in the transverse direction owing to the opposite unidirectional heat-squeeze effect while random Fe_2B grains can be produced under ordinary solidification conditions. The nonoriented Fe_2B intermetallic has the highest linear expansion coefficient of 13.04×10^{-6} °C^{-1} while the microhardness and fracture toughness of transverse Fe_2B intermetallic in the (002) plane are larger than those of Fe_2B with other grain orientations and their values are ~18.72 GPa and 6.42 MPa·$m^{1/2}$, respectively. Liquid zinc corrosion results indicate that unidirectional Fe_2B intermetallic with long axis perpendicular to the direction of liquid zinc corrosion displays the best corrosion resistance to liquid zinc owing to its beneficial barrier effect. The FeB transition phase can naturally form and grow parabolically during liquid zinc corrosion.

I. INTRODUCTION

Thermochemical boriding of iron alloys has been applied to fabricate good wear- and corrosion-resistant materials as an effective surface treatment method.[1,2] In the boriding process, iron borides with both monophase Fe_2B and FeB-based polyphase coatings can be obtained by diffusing boron atoms into the surface of metallic materials and then used mainly to improve the surface hardness and wear resistance of the components for tribological applications.[3–6] Besides, the boriding layers or boride-containing iron alloys show good corrosion resistance to liquid zinc owing to their nonwetting with liquid zinc and therefore can be utilized for planting in the surface of the components as a wear-resistant or corrosion-resistant working layer for corrosion equipment of continuous galvanizing lines or aluminum–zinc die casting mold.[7–11]

Recently, much attention has been paid to boride-based coatings or Fe_2B-containing iron alloys because of their good corrosion resistance in a molten zinc bath.[7–9] Fe_2B intermetallic possessing good thermal stabilization, wear, and corrosion resistance is always introduced into materials as an important skeleton constitution to resist corrosion or wear, and it can be used as a working layer imbedded into the surface of components for applications (i.e., the wear- and corrosion-resistant working layer).[10,11] According to the studies,[7–11] it can be revealed that Fe_2B intermetallic has an improved corrosion resistance in molten zinc. The interaction or synergetic effect between Fe_2B corrosion-resistant skeleton and ductile iron matrix of Fe–B alloy resisting liquid zinc has been systematically investigated.[9,10]

In addition, some investigations have revealed the effects of boride or carbide anisotropy on wear and

Contributing Editor: Jürgen Eckert
[a]Address all correspondence to this author.
e-mail: sqma@mail.xjtu.edu.cn
DOI: 10.1557/jmr.2014.383

 © Materials Research Society 2015

https://doi.org/10.1557/jmr.2014.383 Published online by Cambridge University Press

corrosion resistance, while others reveal no significant effect of carbide anisotropy on wear resistance using a three-body abrasion test under low-stress conditions.[12–16] Moreover, Ti-containing borides display anisotropy on thermal expansion coefficient (TEC) and elastic moduli along different grain orientations.[17] Yin et al. reveal that Fe_2B can transform into a FeB phase in the Zn–Fe–B system when corroded in liquid zinc.[18] Besides, in previous research, the preparation of bulk Fe_2B crystal by using mechanical ball milling and plasma activated sintering was studied, and the fracture toughness of sintered Fe_2B was also measured.[19]

Nevertheless, there is little research on the influence of Fe_2B-grain orientation on its microstructure and properties. In this study, we investigate the microstructure and properties of as-cast bulk Fe_2B intermetallic with various grain orientations, and the effects of Fe_2B-grain orientation on anisotropy of its properties have also been discussed to understand the microstructural and behavioral variations of iron boride. Accordingly, the dependent microstructure–property relationship of bulk Fe_2B intermetallic has been discussed.

II. EXPERIMENTAL PROCEDURES

According to Fe/B ratio (2:1) in the Fe_2B molecular formula, bulk Fe_2B intermetallic in the present work was fabricated in a ZG-5-type vacuum medium frequency induction melting furnace with a vacuum degree of 1 Pa. The initial materials were clean pure iron and Fe–19.55 wt% B ferroalloy. Figure 1 shows a schematic diagram of the directional solidification device with a longitudinal thermal gradient to obtain unidirectional solidified microstructure of Fe_2B intermetallic. The device of directional solidification consists of a copper permanent mold cooled with circulating water and a wrapper of sodium silicate-CO_2 bonded sand with exothermal materials. The oriented and nonoriented Fe_2B intermetallics were melted at 1480–1520 °C and then poured into a sand mold at 1430 °C, respectively, to solidify the desired microstructures. Randomly oriented grains of small size next to the wall of permanent mold (i.e., equiaxed grain zone) were removed 3 mm, and only large columnar grains were used as the oriented alloys. The chemical composition of Fe_2B intermetallic is listed in Table I.

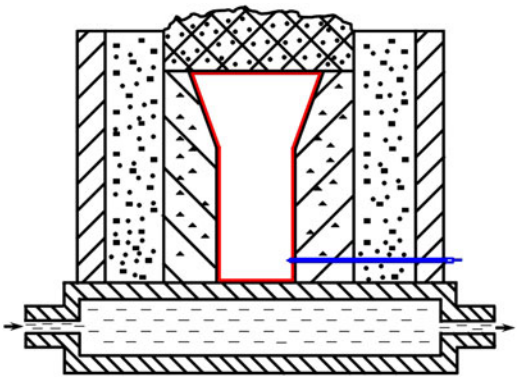


FIG. 1. Schematic device of directional solidified bulk Fe_2B intermetallic (solidification rate of about 17 °C measured by a thermocouple).

Thermal expansion properties of bulk Fe_2B intermetallic were measured using a PCY-II type thermal dilatometer. The dimensions of Fe_2B intermetallic for linear expansion measurement are 50 mm in length and 5 mm in diameter. The heating rate of the tested specimens was 5 °C min^{-1}, and the testing temperature ranged from 350 to 600 °C.

Microhardness of Fe_2B intermetallic was determined by means of an HXD-type 1000 TMC/LCD Vikers-hardness tester with a load of 300 gf. Rectangular bars for fracture toughness test of Fe_2B intermetallic were cut using an electro-discharge machine. Single edge notched bend specimens with V-notch precrack of a/W ratio about 0.5 were ground and polished to the final dimensions of 3 mm × 5 mm × 20 mm. Then, the fracture toughness was measured by using a three-point bending test (INSTRON-1195) with a cross-head speed of 0.5 mm min^{-1}. The fracture toughness K_{IC} can be characterized by using Eqs. (1) and (2) following the ASTM E399 test standard.[19,20]

$$K_{IC} = Y\frac{3PL}{2bW^2}a^{1/2} \quad , \tag{1}$$

$$Y = 1.93 - 3.07\frac{a}{W} + 14.53\left(\frac{a}{W}\right)^2 - 25.11\left(\frac{a}{W}\right)^3 + 25.80\left(\frac{a}{W}\right)^4 \quad , \tag{2}$$

where Y is the geometrical factor related to the crack depth ratio, P is the maximum load, b is the width of the bar, L is the length of the bar, W is the thickness of the bar, and a is the initial crack length.

Corrosion test of Fe_2B intermetallic in liquid zinc was carried out at the temperature of 460 °C. The size of tested samples ground by 2000 mesh carborundum paper was 75 mm × 10 mm × 4 mm, dipped into liquid zinc for

TABLE I. Chemical composition of Fe_2B analyzed via a spark emission spectrometer (wt%).

Element	Sample
B	8.83
Si	2.04
Al	0.08
C	0.07
S	0.015
P	0.021
Fe	Bal.

https://doi.org/10.1557/jmr.2014.383 Published online by Cambridge University Press

40 mm in depth. The volume of liquid zinc for corrosion test was 2.5×10^{-3} m^3 (melting about 17 kg pure zinc), and the immersion corrosion test was carried out under the static condition. Corrosion depth was obtained using a thickness-loss method followed by investigations.[10,21,22] Then, the corrosion rate is characterized as follows (Eq. (3)) (Refs. 8–10, 21, and 22):

$$R = \frac{a - b}{2t} \quad , \tag{3}$$

where R is the corrosion rate ($mm \cdot h^{-1}$), a is the original thickness (mm), b is the final thickness (mm), and t is the corrosion time (h). The factor of 1/2 in the equation is used to reflect the fact that the average thickness change of the sample is caused by the corrosion of both faces of the sample.

The microanalysis on samples was carried out by using an optical microscope (OM), a scanning electron microscope with backscattered electron image (BEI), x-ray diffraction (XRD), electron probe microanalysis (EPMA) equipped with energy dispersive x-ray and wave length dispersive x-ray (WDX) analysis to identify microstructures. For metallographic observations, all samples were etched in a 4 vol% nital solution. XRD was performed on a MXP21VAHF diffractometer with copper K_α radiation as an x-ray source using continuous scanning at 40 kV and 200 mA. The corroded sample was scanned in 2θ ranging from 20° to 60° with a scanning speed of $2° \cdot min^{-1}$ and a step space of 0.02°.

III. RESULTS AND DISCUSSION

A. Effect of orientation on microstructure

Figure 2 shows an optical microstructure of the as-cast bulk Fe_2B intermetallic. From Fig. 2(a), it can be observed that the transverse section of unidirectional solidified Fe_2B intermetallic shows rectangle-shaped grains with the mean size of 14.1 μm in length and 5.8 μm in width, while the longitudinal section shows columnar grains with the growth direction opposite to the heat-squeeze direction [Fig. 2(b)]. However, the ordinary microstructure of non-oriented Fe_2B intermetallic by a casting method is random oriented grains (i.e., equiaxed grains) and the grain size is somewhat heterogeneous [Fig. 2(c)]. Moreover, a little Si-containing compound is found at the grain boundary among Fe_2B grains, which is formed owing to the presence of about 2 wt% Si element in the raw materials of ferroboron.[23–25]

Figure 3 shows XRD analysis of Fe_2B intermetallic. It can be seen that a remarkably strong peak of the (002) plane is detected from Fe_2B crystal in the transverse section (JCPDS 36-1332). Nevertheless, the (002) peak

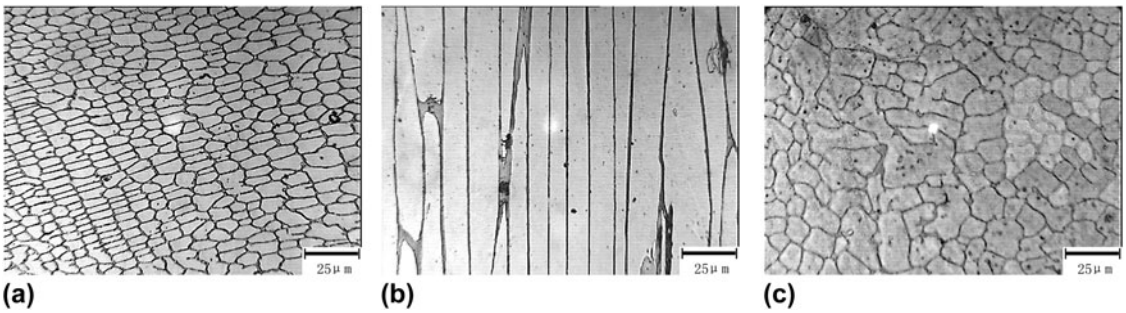


FIG. 2. Optical microstructure of the as-cast bulk Fe_2B intermetallic: (a) Transverse section; (b) longitudinal section; and (c) nonoriented section.

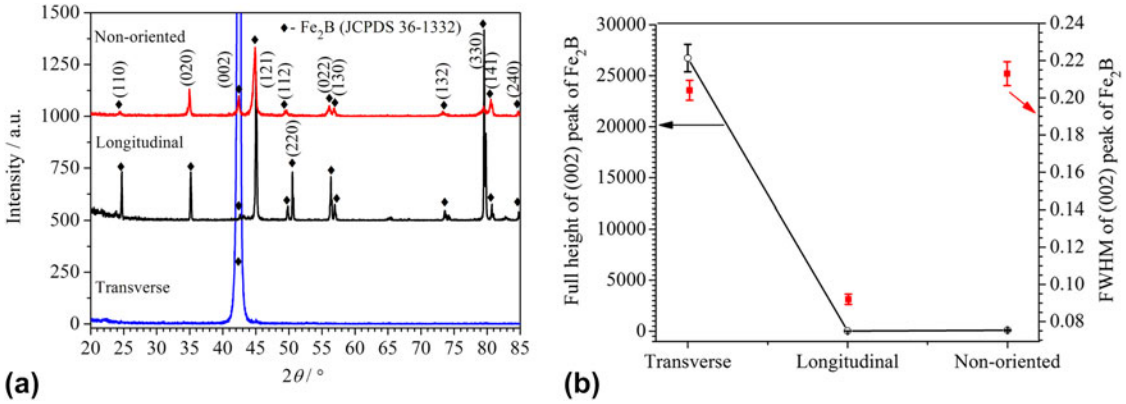


FIG. 3. XRD analysis of bulk Fe_2B intermetallic: (a) XRD pattern and (b) full height and FWHM of (002) peaks for Fe_2B.

https://doi.org/10.1557/jmr.2014.383 Published online by Cambridge University Press

in a longitudinal section is evidently disappeared and the (002) peak of nonoriented Fe_2B also becomes very weak [Fig. 3(a)]. It indicates that unidirectional solidified Fe_2B intermetallic shows obviously textured structure and its preferred growth direction is [002] orientation owing to orthorhombic structure of Fe_2B.[7–10] Figure 3(b) shows the full height and full width at half maximum (FWHM) of (002) peaks of Fe_2B from XRD results in Fig. 3(a). It further suggests that strong Fe_2B textured grains can form along their longitudinal axis and the [002] orientation is the preferred growth direction owing to the opposite heating squeezed direction (i.e., orthorhombic structure of Fe_2B with $a = b = 0.5109$ nm and $c = 0.4249$ nm determined by experimental d space from XRD data).

A little Si-rich compound formed at grain boundaries is detected by WDX analysis listed in Table II. According to the Fe–Si–B ternary phase diagram and other studies,[23,24] the Si-rich compound is determined to be Fe_5SiB_2 phase, which contains 8.53 wt% Si discovered in many investigations.[23–25]

B. Effect of orientation on thermal expansion property

Figure 4 displays the thermal expansion property of Fe_2B intermetallic. It can be seen that although the linear expansion displacement of a longitudinal sample is much larger than that of transverse and nonoriented samples as the temperatures range from 350 to 600 °C [as shown in Fig. 4(a)], the slope of linear expansion displacement of nonoriented Fe_2B intermetallic is much higher than that of oriented Fe_2B intermetallic (i.e., transverse and longitudinal samples). According to TEC shown in Fig. 4(b), the TEC values of bulk Fe_2B intermetallic are 11.04×10^{-6}, 10.00×10^{-6}, and 13.04×10^{-6} °C^{-1} for transverse, longitudinal, and nonoriented Fe_2B grains, respectively. It reveals that the thermal expansion property of Fe_2B intermetallic can be strongly affected by Fe_2B grain orientation which may be related to the atomic spatial distribution of Fe_2B crystal.[17,26]

According to the crystal structure of Fe_2B with a space group of $I4/mcm$ (No. 140) and bbc tetragonal structure (C16, $CuAl_2$-type), eight Fe atoms are in general position (8h site along z-axis by 0.25c and 0.75c and also along x- and y-directions by 0.5a and 0.5b in Fe_2B cell), while four B atoms are in special position (4a site).[17,27] Therefore, the atomic density of boron along the c-direction (i.e., [002] direction) is higher than that of Fe atom, and it leads to the smaller atomic thermal motion and thermal expansion property along the longitudinal direction compared with other orientations (i.e., transverse and nonoriented samples) owing to more B–B covalent bond.[17] On the other hand, the thermal expansion property may be affected by lattice dynamical properties and thermal–physical properties of Fe_2B cell volume along various orientations caused by phonon dispersion. Sun reveals that Ti-borides possess different CETs along [100], [010], and [001] orientations owing to anharmonic effect of the thermal energy of lattice vibration, which brings

TABLE II. Electron microprobe analysis of borides in bulk Fe_2B intermetallic.

	Element (wt%)			Element (at.%)					
Phase	Fe	Si	B	Fe	Si	B	Si/Fe ratio	Crystal structure	Calculated formula
Fe_2B	91.02	0.07	8.91	66.67	0.10	33.23	0.00	Tetragonal	Fe_2B (Si)
Fe_5SiB_2	84.42	8.53	7.05	61.46	12.42	26.12	0.20	Tetragonal	$Fe_{4.71}Si_{0.95}B_2$

%B is given by difference. The values are based on an average of 10 different areas per sample.

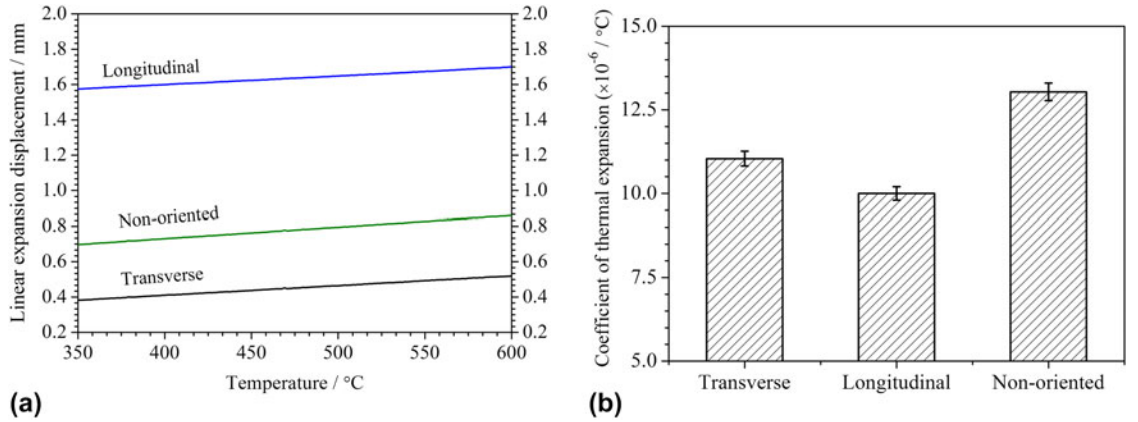


FIG. 4. Thermal expansion property of Fe_2B intermetallic with various grain orientations: (a) Linear expansion displacement and (b) TEC.

https://doi.org/10.1557/jmr.2014.383 Published online by Cambridge University Press

about volumetric coefficient variation.[17,28] That is to say, the anharmonic effect of lattice vibration for Fe_2B intermetallic with various grain orientations may probably result in the differences of thermal expansion property along different Fe_2B orientations as shown in Fig. 4. In addition, the anharmonic effect of lattice vibration may be significantly influenced by various defects in Fe_2B intermetallic with various crystal orientations such as vacancies and site disorder.[17,29] Therefore, Fe_2B intermetallic along [002] orientation can generate a small thermal energy of lattice vibration compared to other crystal orientations in oriented Fe_2B intermetallic, while nonoriented grains of Fe_2B intermetallic may achieve more lattice dynamical properties according to the special structure and distribution of random Fe_2B cell.

C. Effect of orientation on microhardness and fraction toughness

Figure 5 shows the microhardness and fracture toughness of bulk Fe_2B intermetallic. From Fig. 5(a), it is clear that transverse Fe_2B intermetallic possesses the highest Vickers hardness value (~18.72 GPa) compared with longitudinal and nonoriented Fe_2B intermetallics (~17.85 and ~18.14 GPa, respectively), which is related to atom bounding energy of different crystal planes of Fe_2B lattice.[26,27] From Fig. 5(b), the fracture toughness of the as-cast Fe_2B intermetallic ranges from 5.97 to 6.42 MPa·m$^{1/2}$ when loaded along various Fe_2B orientations (i.e., transverse, longitudinal, and nonoriented sections, respectively), which is higher than that of sintered bulk Fe_2B owing to the presence of a few pores among them. Moreover, the fracture toughness of transverse Fe_2B intermetallic is larger than that of longitudinal and nonoriented Fe_2B, which is attributed to the inherent brittleness vertical to the [002] orientation of Fe_2B.[26,27] Thus, more microcracks may be produced vertical to the [002] orientation under a deformation process.[26,30] Many investigations were carried out to investigate the large inherent brittleness perpendicular to the [002] orientation and sensibility of microcracking because of the weaker B–B covalent bond and bounding energy as well as the interaction of iron and boron atoms, which also results from the spatial heterogeneous distribution of Fe and B atoms in Fe_2B lattice.[26,27,31,32] Therefore, bulk Fe_2B intermetallic with various orientations displays strongly anisotropy. Besides, the configurations or hybridizations of atomic orbitals depending on energy differences and symmetric properties of Fe and B in Fe_2B cell may remarkably affect the mechanical properties related to its chemical structure, such as bulk modulus and fracture toughness.[17,27–29] From Figs. 5(c) and 5(d), there are more tearing and local slipping characteristics on the (002) plane when loaded vertically. Due to the strong bounding energy and small microcracking of Fe_2B intermetallic on the (002) plane,

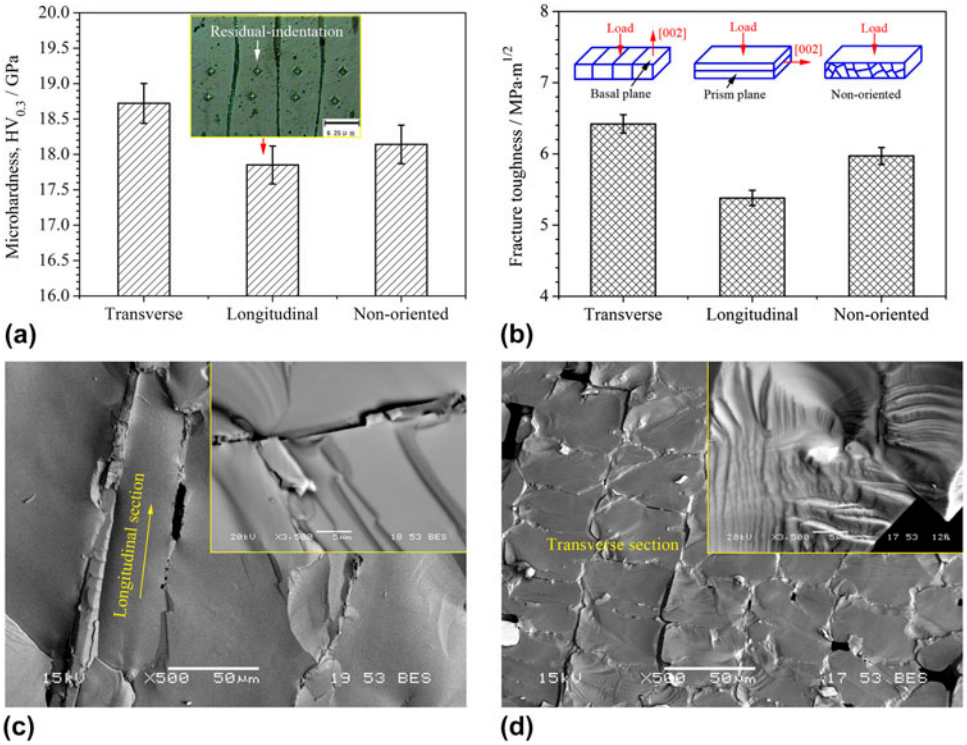


FIG. 5. Microhardness and fracture toughness of bulk Fe_2B intermetallic: (a) Vickers hardness; (b) fracture toughness; (c) transverse fracture; and (d) longitudinal fracture.

https://doi.org/10.1557/jmr.2014.383 Published online by Cambridge University Press

the microhardness and fracture toughness are largest along the [002] orientation.[26,27] Hence, the differences among various orientations for Fe_2B intermetallic depend on not only lattice structures but also microcracking sensibility of Fe_2B.

D. Effect of orientation on corrosion resistance to liquid zinc

Figure 6 shows corrosion resistance and OM interfacial morphologies of bulk Fe_2B intermetallic with various grain orientations against liquid zinc. From Fig. 6(a), it is obviously found that longitudinal Fe_2B perpendicular to the diffusion direction of liquid zinc has the best corrosion resistance to liquid zinc owing to its beneficial barrier effect and thus strongly restricts the liquid zinc diffusion path compared with the rest orientation samples. On the other hand, the failure of bulk Fe_2B intermetallics with different grain orientations can lead to various corrosion interfaces and corrosion process as well as the occurrence of microcracks around the corrosion interface.[8,10] According to interfacial morphologies from Figs. 6(b)–6(d), it is clear that there exists a transition layer close to the inner Fe_2B substrate except for Fe–Zn compounds (mainly ζ-$FeZn_{13}$).[8,10,21] The transition layer in a transverse sample displays an interlocking shape overlain at the interface with a mean width of ~30 μm, while it is lath-shaped in the longitudinal sample with an interface of ~20 μm thickness, which is approximate to the grain width of longitudinal Fe_2B. Meanwhile, an obvious intergranular corrosion along the grain boundary is observed for nonoriented sample with a corrosion thickness of ~30 μm. Therefore, the grain orientation of Fe_2B intermetallic can markedly create different interfacial morphologies and result in various corrosion resistances in liquid zinc, which is mainly attributed to various zinc diffusion paths and zinc concentrations following the above corrosion manners.

Figure 7 shows the XRD result of bulk Fe_2B intermetallic corroded in liquid zinc. It is found that some FeB phases indexed by JCPDS 32-0463 and/or 65-2599 can be accurately detected except for ζ-$FeZn_{13}$ (JCPDS 65-1238), δ-$FeZn_{10}$ (JCPDS 65-1238), and the residual Fe_2B (JCPDS 36-1332) in corrosion layers, which is well agreed with other investigations.[8,10,18,21]

Figure 8 shows BEI morphologies and EPMA line analysis of corrosion layers. It reveals that zinc corrosion can mainly proceed along columnar grain boundaries of transverse Fe_2B intermetallic as shown in Fig. 8(a), and some cracks generate through the width direction of bulk Fe_2B grains accompanying slight dissolution of Fe_2B and formation of transition layer FeB phase

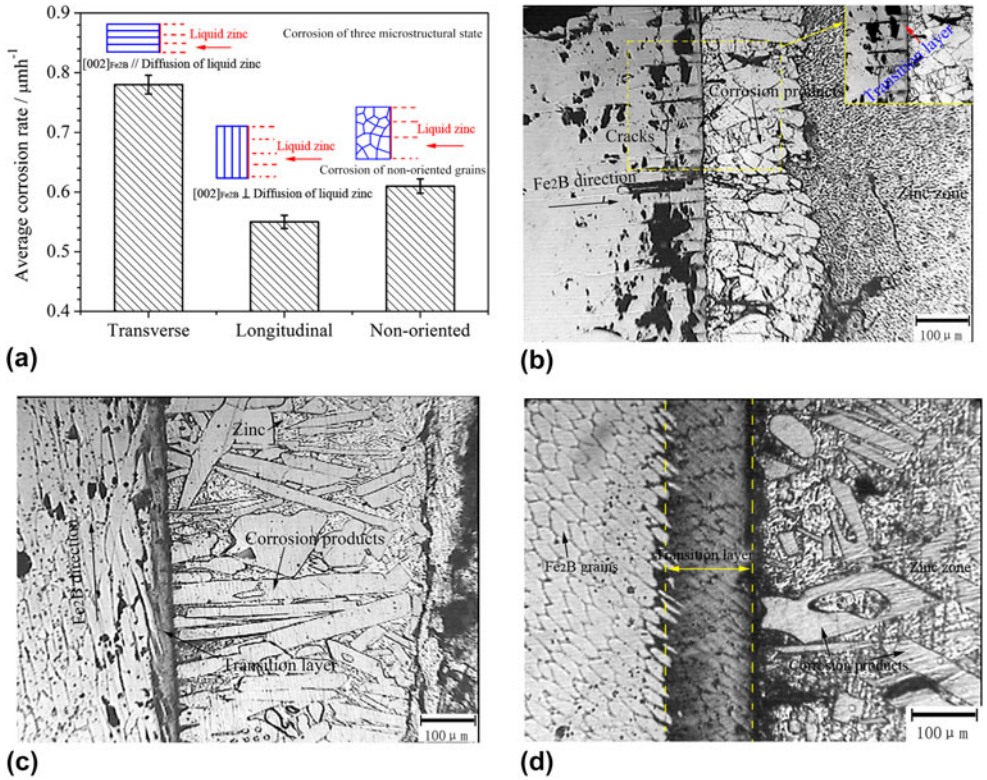


FIG. 6. Corrosion rate and OM interfacial morphologies of bulk Fe_2B intermetallic in liquid zinc under static condition: (a) Corrosion rate; (b) OM interfacial morphologies of transverse section; (c) OM interfacial morphologies of longitudinal section; and (d) OM interfacial morphologies of nonoriented section.

https://doi.org/10.1557/jmr.2014.383 Published online by Cambridge University Press

detected by XRD.[8,10,18,33] However, a layer-by-layer corrosion vertical to the longitudinal section of Fe_2B occurs and the gray transition layer also forms as shown in Fig. 8(b). Clearly, some ζ-$FeZn_{13}$ is found near the surface of corrosion layers. It indicates that the corrosion of Fe_2B in liquid zinc may result in the strong release of free Fe atom to form gray transition layer FeB phase under high zinc chemical potential according to lattice reorganization.[18,22] Simultaneously, partial released Fe can combine with Zn atom to form ζ-$FeZn_{13}$ phase as reported by other studies.[18,22,34] From the corrosion of nonoriented Fe_2B grains in Fig. 8(c), it is clear that many Fe_2B grains are corroded by liquid zinc, and grain-boundary corrosion is intensively dominant in liquid zinc. The corroded Fe_2B in corrosion layers and the corresponding EPMA analysis along line segment AB on spalling Fe_2B surrounded by liquid zinc in Fig. 8(d) reveal that the peripheral gray transition layer of corroded Fe_2B possesses a uniform Fe content, and there is a sharp linear decrease of Fe at the Fe_2B/transition layer interface [I-zone/II-zone interface and II-zone/III-zone interface shown in Fig. 8(d)]. It further suggests that the uniform

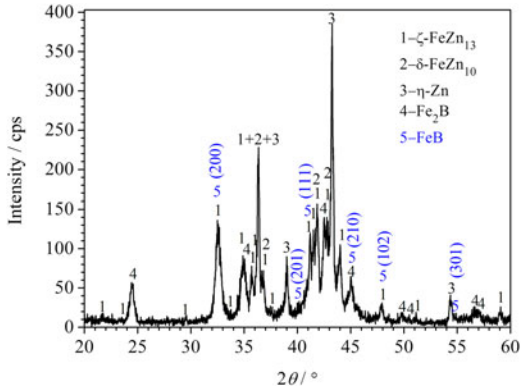


FIG. 7. XRD result of corrosion layer for Fe_2B intermetallic corroded in liquid zinc.

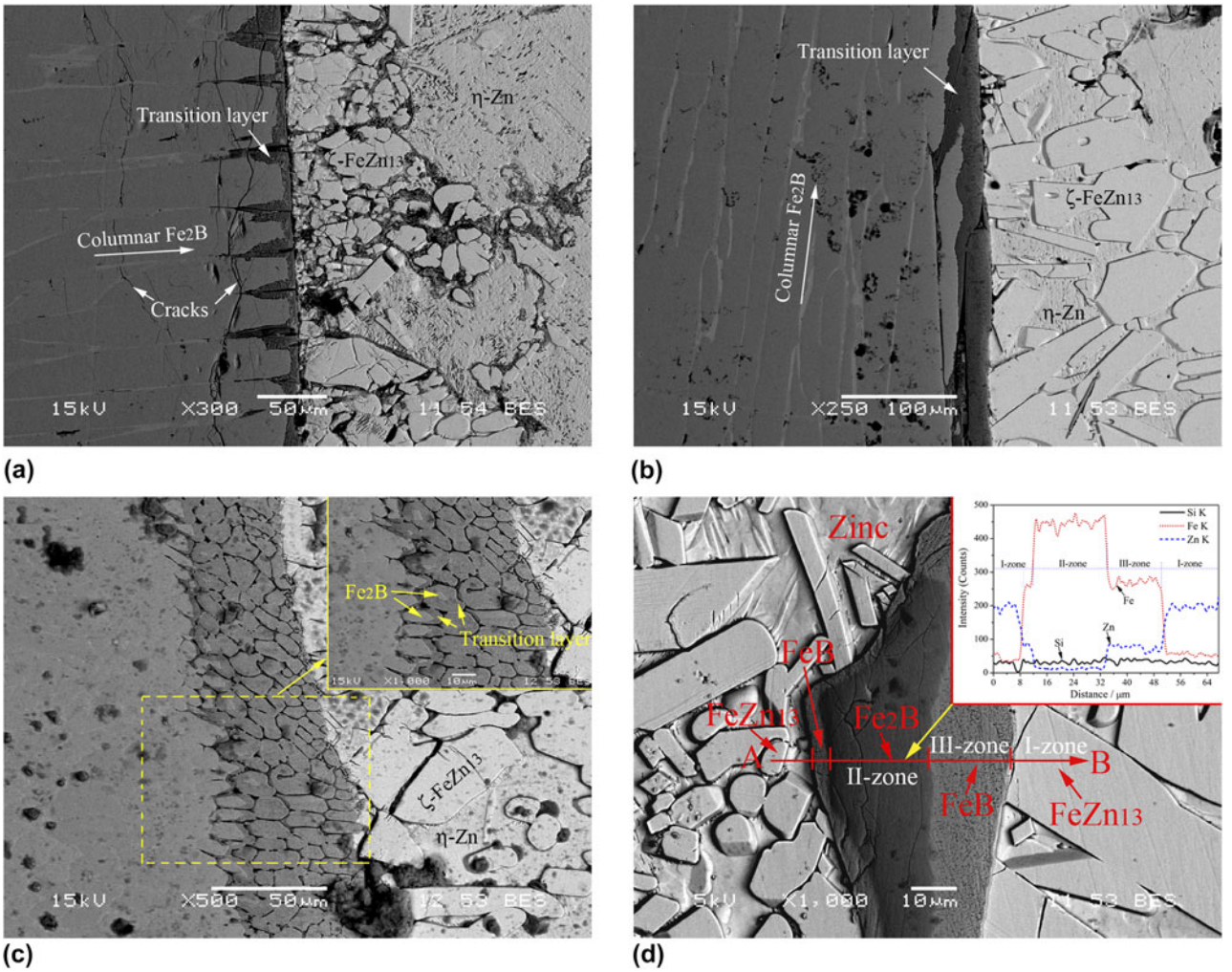


FIG. 8. BEI morphologies and EPMA line analysis of bulk Fe_2B intermetallic in liquid zinc: (a) Transverse section; (b) longitudinal section; (c) nonoriented section; and (d) spalling Fe_2B surrounded by liquid zinc and corresponding EPMA analysis along line segment AB in corrosion layers.

https://doi.org/10.1557/jmr.2014.383 Published online by Cambridge University Press

FeB compound in a transition layer can naturally form.[18,22] From the analysis above, the crucial corrosion process of all bulk Fe_2B with various orientations in liquid zinc includes slight dissolution and main phase transition process from Fe_2B to FeB intermetallic, which governs the corrosion of bulk Fe_2B in liquid zinc.

Figure 9 shows the growth thickness of FeB intermetallic compound (IMC) transformed from Fe_2B intermetallic in liquid zinc corrosion. It can be seen that the growth thickness of all Fe_2B with various orientations conforms to the law of approximately parabolic increase.[35] Besides, the longitudinal Fe_2B perpendicular to diffusion direction of liquid zinc (i.e., liquid zinc corrosion direction) has the slowest growth thickness compared to samples with other Fe_2B orientations, which is ascribed to a small corrosion path and beneficial barrier effect of Fe_2B generated by grain orientations.

According to the Zn–Fe–B system reported by Yin,[18] a coexisting phase of FeB, ζ-$FeZn_{13}$, and η-Zn can be established. WDX results listed in Table III also reveal that the gray transition layer is FeB phase and it is supersaturated with zinc atom, which is well agreed with XRD result and other investigations.[18,22] Based on the microstructural analysis and observations on interfaces, it can be confirmed that zinc corrosion of bulk Fe_2B intermetallic remarkably not only depends on grain orientation of Fe_2B but also is affected by dissolution and FeB phase transition produced from zinc potential or concentration.

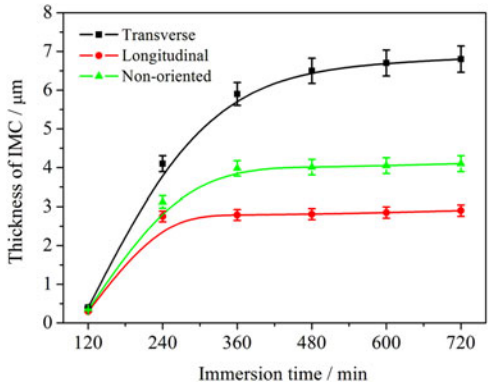


FIG. 9. Growth thickness of FeB IMC transformed from Fe_2B intermetallic during liquid zinc corrosion.

TABLE III. Average composition of substrate (bulk Fe_2B intermetallic) and corrosion layers (transition layer and Fe–Zn layer) measured via WDX analysis at 20 different areas.

	Element (at.%)					
Analysis zone	Fe	Zn	Si	B	Fe/B ratio	Determined phase
Substrate	66.68	0.00	0.12	33.20	2.00	Fe_2B (Si)
Transition layer	48.27	11.08	1.37	39.28	1.23	FeB (Zn, Si)
Fe–Zn product	93.95	6.05	0.00	0.00	None	$FeZn_{13}$

%B is given by difference. The values are based on an average of 20 different areas per samples.

IV. CONCLUSIONS

This study investigates the effects of crystal orientation on microstructure and properties of bulk as-cast Fe_2B intermetallic. The results obtained are as follows.

(1) The unidirectional solidified Fe_2B intermetallic possesses a strong (002) texture in the transverse direction with a mean grain size of 14.1 μm in length and 5.8 μm in width while random Fe_2B grains produce under ordinary solidification conditions.

(2) The nonoriented Fe_2B intermetallic has the highest linear expansion coefficient of 13.04×10^{-6} °C^{-1} while the microhardness and fracture toughness of transverse Fe_2B intermetallic are larger than that with other grain orientations and their values are ~18.72 GPa and 6.42 MPa·$m^{1/2}$, respectively.

(3) Liquid zinc corrosion results indicate that unidirectional Fe_2B intermetallic with Fe_2B long axis perpendicular to the direction of liquid zinc corrosion displays the best corrosion resistance to liquid zinc owing to its beneficial barrier effect. The transition phase FeB can naturally form and parabolically grow during liquid zinc corrosion.

ACKNOWLEDGMENTS

The authors thank the financial support for this work from the Natural Science Foundation of China under Grant Nos. 51271142, 51301128, & 51274016, the Specialized Research Fund for the Doctoral Program of Higher Education of China under Grant Nos. 20110201130008 & 20120201120005, the National Science Foundation for Post-doctoral Scientists of China under Grant Nos. 2012M521767 & 2013T60875, the Natural Science Foundation of Shaanxi Province under Grant No. 2014JQ7281, the Shaanxi provincial post-doctoral research project, and the Fundamental Research Funds of Xi'an Jiaotong University under Grant Nos. xjj2013038 & xjj2014167.

REFERENCES

1. V.I. Dybkov, W. Lengauer, and K. Barmak: Formation of boride layers at the Fe-10%Cr alloy-boron interface. *J. Alloys Compd.* **398**, 113 (2005).
2. Z. Hu, Y. Fan, Y. Wu, Q. Yan, and Y. Chen: Crystallization and structure of high boron content iron-boron ultrafine amorphous alloy particles. *J. Mater. Sci.* **31**, 611 (1996).
3. O. Ozdemir, M. Usta, C. Bindal, and A. Ucisik: Hard iron boride (Fe_2B) on 99.97wt% pure iron. *Vacuum* **80**, 1391 (2006).
4. U. Sen, S. Sen, S. Koksal, and F. Yilmaz: Fracture toughness of borides formed on boronized ductile iron. *Mater. Des.* **26**, 175 (2005).

https://doi.org/10.1557/jmr.2014.383 Published online by Cambridge University Press

5. S. Taktak: Some mechanical properties of borided AISI H13 and 304 steels. *Mater. Des.* **28**, 1836 (2007).
6. Y. Kayali, S. Taktak, S. Ulu, and Y. Yalcin: Investigation of mechanical properties of boro-tempered ductile iron. *Mater. Des.* **31**, 1799 (2010).
7. D.N. Tsipas, G.K. Triantafyllidis, K.J. Kiplagat, and P. Psillaki: Degradation behaviour of boronized carbon and high alloy steels in molten aluminium and zinc. *Mater. Lett.* **37**, 128 (1998).
8. S.Q. Ma, J.D. Xing, H.G. Fu, D.W. Yi, X.H. Zhi, and Y.F. Li: Effects of boron concentration on the corrosion resistance of Fe-B alloys immersed in 460 °C molten zinc bath. *Surf. Coat. Technol.* **204**, 2208 (2010).
9. S.Q. Ma, J.D. Xing, D.W. Yi, H.G. Fu, J.J. Zhang, Y.F. Li, Z.Y. Zhang, G.F. Liu, and B.J. Zhu: Interfacial morphology and corrosion resistance of Fe-B cast steel containing chromium and nickel in liquid zinc. *Corros. Sci.* **53**, 2826 (2011).
10. S.Q. Ma, J.D. Xing, D.W. Yi, H.G. Fu, J.J. Zhang, Y.F. Li, Z.Y. Zhang, G.F. Liu, and B.J. Zhu: Microstructure and corrosion behavior of cast Fe-B alloys dipped into liquid zinc bath. *Mater. Charact.* **61**, 866 (2010).
11. D.N. Tsipas and J. Rus: Boronizing of alloy steels. *J. Mater. Sci. Lett.* **6**, 118 (1987).
12. D.W. Yi, J.D. Xing, S.Q. Ma, H.G. Fu, Y.F. Li, W. Chen, J.B. Yan, J.J. Zhang, and R.R. Zhang: Investigations on microstructures and two-body abrasive wear behavior of Fe-B cast alloy. *Tribol. Lett.* **45**, 427 (2012).
13. Z.F. Huang, J.D. Xing, and C. Guo: Improving fracture toughness and hardness of Fe_2B in high boron white cast iron by chromium addition. *Mater. Des.* **31**, 3084 (2010).
14. J.J. Coronado: Effect of $(Fe,Cr)_7C_3$ carbide orientation on abrasion wear resistance and fracture toughness. *Wear* **270**, 287 (2011).
15. Ö.N. Doğan and J.A. Hawk: Effect of carbide orientation on abrasion of high Cr white cast iron. *Wear* **189**, 136 (1995).
16. S.R. Wang, L.H. Song, Y. Qiao, and M. Wang: Effect of carbide orientation on impact-abrasive wear resistance of high-Cr iron used in shot blast machine. *Tribol. Lett.* **50**, 439 (2013).
17. L. Sun, Y.M. Gao, B. Xiao, Y.F. Li, and G.L. Wang: Anisotropic elastic and thermal properties of titanium borides by first-principles calculations. *J. Alloys Compd.* **579**, 457 (2013).
18. F.C. Yin, X.L. Ruan, M.X. Zhao, Y.X. Liu, and Z. Li: The 600 °C and 450 °C isothermal sections of the Zn-Fe-B system. *J. Alloys Compd.* **565**, 79 (2013).
19. Z.F. Huang, S.Q. Ma, J.D. Xing, and B.Y. Wang: Bulk Fe_2B crystal fabricated by mechanical ball milling and plasma activated sintering. *J. Alloys Compd.* **582**, 196 (2014).
20. W.C. Liu, L.K. Jiang, L. Cao, J. Mei, G.H. Wu, S. Zhang, L. Xiao, S.H. Wang, and W.J. Ding: Fatigue behavior and plane-strain fracture toughness of sand-cast Mg-10Gd-3Y-0.5Zr magnesium alloy. *Mater. Des.* **59**, 466 (2014).
21. W.J. Wang, J.P. Lin, Y.L. Wang, and G.L. Chen: The corrosion of Fe_3Al alloy in liquid zinc. *Corros. Sci.* 1340 (2007).
22. S.Q. Ma, J.D. Xing, H.G. Fu, Y.L. He, Y. Bai, Y.F. Li, and Y.P. Bai: Interface characteristics and corrosion behaviour of oriented bulk Fe_2B alloy in liquid zinc. *Corros. Sci.* **78**, 71 (2014).
23. V. Raghavan: B-Fe-Si (boron-iron-silicon). *J. Phase Equilib. Diffus.* **28**, 380 (2007).
24. B. Aronsson and I. Engström: X-ray investigations on Me-Si-B systems (Me=Mn, Fe, Co). II. Some features of the Fe-Si-B and Mn-Si-B systems. *Acta Chem. Scand.* **14**, 1403 (1960).
25. Y. Li and R.P.H. Chang: Synthesis and characterization of iron silicon boron (Fe_5Si_2B) and iron boride (Fe_3B) nanowires. *J. Am. Chem. Soc.* **128**, 12778 (2006).
26. M.S. Li, S.L. Fu, W.D. Xu, R.L. Zhang, and R.H. Yu: Valence electron structure of Fe_2B phase and its eigen-brittleness. *Acta Metall. Sin.* **31**, 201 (1995).
27. B. Xiao, J.D. Xing, S.F. Ding, and W. Su: Stability, electronic and mechanical properties of Fe_2B. *Phys. B* **403**, 1723 (2008).
28. A. Van de Walle and G. Ceder: The effect of lattice vibrations on substitutional alloy thermodynamics. *Rev. Mod. Phys.* **74**, 11 (2002).
29. A.A. Quong and A.Y. Liu: First-principles calculations of the thermal expansion of metals. *Phys. Rev. B* **56**, 7767 (1997).
30. E. Hernández-Sanchez, G. Rodriguez, A. Meneses-Amador, D. Bravo-Bárcenas, I. Arzate-Vazquez, H. Martínez-Gutiérrez, M. Romero-Romo, and I. Campos-Silva: Effect of the anisotropic growth on the fracture toughness measurements obtained in the Fe_2B layer. *Surf. Coat. Technol.* **237**, 292 (2013).
31. C.Q. Guo: Modeling of spatial distribution of the eutectic M_2B borides in Fe-Cr-B cast irons. *J. Mater. Sci.* **39**, 1109 (2004).
32. S.Q. Ma, J.D. Xing, G.F. Liu, D.W. Yi, H.G. Fu, J.J. Zhang, and Y.F. Li: Effect of chromium concentration on microstructure and properties of Fe-3.5B alloy. *Mater. Sci. Eng., A* **527**, 6800 (2010).
33. W.J. Wang, J.P. Lin, Y.L. Wang, and G.L. Chen: The corrosion of intermetallic alloys in liquid zinc. *J. Alloys Compd.* **428**, 237 (2007).
34. A.R. Marder: The metallurgy of zinc-coated steel. *Prog. Mater. Sci.* **45**, 191 (2000).
35. V.I. Dybkov and O.V. Duchenko: Growth kinetics of compound layers at the nickel-bismuth interface. *J. Alloys Compd.* **234**, 295 (1996).

https://doi.org/10.1557/jmr.2014.383 Published online by Cambridge University Press